PAPER

Cilostazol-imprinted polymer film-coated electrode as an electrochemical chemosensor for selective determination of cilostazol and its active primary metabolite†

Jyoti,[a] Renata Rybakiewicz-Sekita,[bc] Teresa Żołek,[d] Dorota Maciejewska,[d] Edyta Gilant,[e] Katarzyna Buś-Kwaśnik,[e] Andrzej Kutner,[f] Krzysztof R. Noworyta [iD] ⋆[a] and Wlodzimierz Kutner [iD] ⋆[ab]

An electrochemical chemosensor for cilostazol (CIL) determination was devised, engineered, and tested. For that, a unique conducting film of the functionalized thiophene-appended carbazole-based polymer, molecularly imprinted with cilostazol (MIP-CIL), was potentiodynamically deposited on a Pt disk electrode by oxidative electropolymerization. Thanks to electro-oxidation potentials lower than that of CIL, the carbazole monomers outperformed pyrrole, thiophene, and phenol monomers, in this electro-polymerization. The pre-polymerization complexes quantum-mechanical and molecular dynamics analysis allowed selecting the most appropriate monomer from the three thiophene-appended carbazoles examined. The electrode was then used as a selective CIL chemosensor in the linear dynamic concentration range of 50 to 924 nM with a high apparent imprinting factor, IF = 10.6. The MIP-CIL responded similarly to CIL and CIL's pharmacologically active primary metabolite, 3,4-dehydrocilostazol (dhCIL), thus proving suitable for their determination together. Simulated models of the MIP cavities binding of the CIL, dhCIL, and interferences' molecules allowed predicting chemosensor selectivity. The MIP film sorption of CIL and dhCIL was examined using DPV by peak current data fitting with the Langmuir (L), Freundlich (F), and Langmuir–Freundlich (LF) isotherms. The LF isotherm best described this sorption with the sorption equilibrium constant (K_{LF}) for CIL and dhCIL of 12.75×10^{-6} and 0.23×10^{-6} M, respectively. Moreover, the chemosensor cross-reactivity to common interferences study resulted in the selectivity to cholesterol and dehydroaripiprazole of 1.52 and 8.0, respectively. The chemosensor proved helpful in determining CIL and dhCIL in spiked human plasma with appreciable recovery (99.3–134.1%) and limit of detection (15 nM).

1. Introduction

Over the last decades, the number of patients affected by intermittent claudication (IC), an initial symptom of peripheral artery disease (PAD), has increased severely.[1] PAD is a progressive disorder caused by the occlusion of large or medium lower body arteries. Over 200 million people are afflicted by PAD worldwide.[2] Moreover, the cardiovascular and diabetic mortality rate is increased ∼15 fold by IC.[2]

Many different drugs are being administered alone or in combinations to cure this disorder. Cilostazol (CIL) is one of them (Scheme 1). Nowadays, CIL is being studied extensively

[a] Institute of Physical Chemistry, Polish Academy of Sciences, Kasprzaka 44/52, 01-224 Warsaw, Poland. E-mail: knoworyta@ichf.edu.pl, wkutner@ichf.edu.pl

[b] Faculty of Mathematics and Natural Sciences, School of Sciences, Institute of Chemical Sciences, Cardinal Stefan Wyszynski University in Warsaw, Wóycickiego 1/3, 01-815 Warsaw, Poland
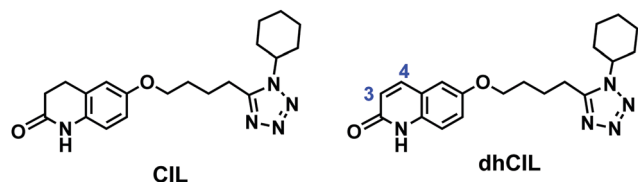
[c] Laboratory of Organic Electronics, Linköping University, Bredgatan 33, 602 21 Norrköping, Sweden

[d] Department of Organic Chemistry, Faculty of Pharmacy, Medical University of Warsaw, Banacha 1, 02-097, Warsaw, Poland

[e] Łukasiewicz Research Network – Industrial Chemistry Institute, Rydygiera 8, 01-793, Warsaw, Poland

[f] Department of Bioanalysis and Drug Analysis, Faculty of Pharmacy, Medical University of Warsaw, Banacha 1, 02-097 Warsaw, Poland

† Electronic supplementary information (ESI) available: The following files are available free of charge. Structural formulas of the functional monomers, simulated structures of pre-polymerization complexes, PM-IRRAS spectra, AFM film images, the tabulated morphological and nanomechanical parameters derived from AFM images, SEM film images, normalized DPV peak current *vs.* CIL concentration for MIP and NIP film-coated electrodes fitted with different isotherms, tabulated parameters of different isotherms fitted to the normalized DPV peak current, skeleton models showing the imprinted cavity interactions with the interferences' molecules, tabulated fitting parameters of Langmuir–Freundlich isotherms, and the table comparing analytical parameters of the present chemosensor with some from literature. (PDF). See DOI: 10.1039/d1tb02186a

This journal is © The Royal Society of Chemistry 2022

J. Mater. Chem. B, 2022, **10**, 6707–6715 | **6707**

Scheme 1 Structural formulas of cilostazol (CIL) and 3,4-dehydro-cilostazol (dhCIL).

because of its effectiveness in PAD curing. CIL is a synthetic quinolinone derivative inhibiting phosphodiesterase III (PDE_3), thereby increasing cyclic adenosine monophosphate (cAMP) phosphodiesterase inhibition of platelet aggregation and cell proliferation.[3,4]

CYP3A4 and CYP2C19 hepatic enzymes oxidatively metabolize CIL into many metabolites. Two of these, namely, 3,4-dehydro-cilostazol (dhCIL) (Scheme 1) and monohydroxycilostazol (not shown), are also responsible for inhibitory effects on platelet aggregation.[5]

Moreover, CIL is considered to treat diseases like Alzheimer's disease (AD),[6] diabetes,[7] strokes,[8] and hypertension.[9] Currently, CIL is undergoing several clinical trials.[10,11] Furthermore, a CASTLE long-term study (Cilostazol: A Study in Long-term Effects, CASTLE) evaluated CIL efficacy and tolerability in PAD patients. Apparently, the peak plasma concentration of orally administered (50 to 200) mg CIL was 806 ($\pm$ 238) μg L^{-1} within 3 h.[12] Interestingly, dhCIL is five times more potent than its CIL parent drug.[13]

Our present study aims at engineering a molecularly imprinted polymer (MIP) electrochemical chemosensor suitable as a potential point-of-care (PoC) tool to determine the CIL concentration in human plasma. PoC devices serve diagnostics that can readily be used in hospitals, airports, and, remarkably, patients at homes because of providing an adequate low limit of detection (LOD), easy use, cost-effectiveness, and a short determination time.[14–16] For the last decade, there has been a tremendous improvement in developing PoC systems to overcome several problems, including long awaiting the determination results and handling sophisticated instruments used in the traditional laboratory analysis.[16] The ASSURED principle is assumed for PoC devices, which stands for affordable, sensitive, selective, user-friendly, rapid and robust, equipment-free, and deliverable to end-user operations.[17] PoC systems have made the patients' lives easier, especially in the diagnosis based on the determination of biomolecular compounds.[18,19] Recently, MIPs have been applied in PoC devices.[20,21]

An MIP is a polymeric, artificial receptor with imprinted molecular cavities serving, among others, as synthetic mimics of antibodies.[22,23] For the last decades, molecular imprinting has been established as an effective procedure where the MIP cavities complement the template molecules in shape, size, and functionalization. Furthermore, MIPs are readily prepared. They are inexpensive, chemically resistant, highly selective, and sensitive, making them attractive for sensing small molecular[24,25] and macromolecular compounds like proteins, nucleic acids, *etc.*,

and in other applications, including diagnosis[25,26] and separation science.[27,28]

So far, tandem-MS with electrospray ionization, EIS, in the positive ion mode,[29] LC-MS/MS, with EIS,[30] HPLC,[31] and spectrofluorimetry[32] have been applied for CIL and dhCIL join determination in human plasma. Although methods that use HPLC and LC-MS/MS are sensitive and selective, they require laborious sample preparation, trained operators, expensive instrumentation, and often time-consuming analyte determination. Hence, a rapid and straightforward method for early CIL detecting and monitoring for overdose diagnoses is needed. Toward that, we herein devised, prepared, and validated an MIP electrochemical chemosensor for sensitive CIL and dhCIL determination as an alternative to optical sensors,[33] enabling powerful yet cost-effective suitable for PoC diagnosis.

Accordingly, we have herein successfully imprinted CIL in a unique functionalized (thiophene-appended carbazole)-based conducting MIP and simultaneously deposited it on an electrode surface as a thin film *via* potentiodynamic electropolymerization. Being user-friendly, selective, sensitive, and allowing the early detection of many disease symptoms,[34,35] electrochemical MIP-using chemosensors can serve as attractive PoC tools. Potentiodynamic electropolymerization is a well-established technique providing a homogenous polymer film coating a transducer, *i.e.*, an electrode in our current study. Likewise, the deposited CIL-templated MIP (MIP-CIL) film was then used as a recognition unit of an electrochemical chemosensor. Herein, we overcome challenges encountered in our previous work[36] by achieving a lower LOD, lower linear dynamic concentration range, ease of sensor preparation, and cross-validation of CIL and dhCIL in a test solution and CIL or dhCIL spiked human plasma by LC-MS. The CIL-extracted MIP-CIL affinity to analytes and interferences was computationally modeled with the complexation and sorption processes' molecular dynamics (MD) simulations.

2. Experimental section

2.1 Materials

CIL, 6-[4-(1-cyclohexyltetrazol-5-yl)butoxy]-3,4-dihydro-1*H*-quinolin-2-one, was from MedChemExpress, whereas ferrocene, tetrabutylammonium perchlorate, (TBA)ClO$_4$, and anhydrous dichloromethane (DCM) of electrochemical grade were from Sigma-Aldrich. Analytical grade NaOH was from Chempur. The dehydroaripiprazole-d8 and dhCIL reference standards for bioanalysis were from Toronto Research Chemicals, Canada.

2.2 Instrumentation, techniques, and procedures

Instrumentation used is described in Section S1 in ESI.† Moreover, ESI,† provides other details, including syntheses and depositions of MIP and non-imprinted polymer (NIP) films, preparation of CIL or dhCIL spiked human plasma samples for the LC-MS and electrochemical measurements. Moreover, chemosensors' selectivity to interferences and computer simulations details are described.

3. Results and discussion

3.1 Selecting functional monomers

Chemosensors with an MIP film as the recognition unit should recognize the target analyte with sufficient selectivity, detectability, and sensitivity. That is only possible if the analyte appropriately interacts with the MIP. Interactions in the pre-polymerization complex solution can define MIP properties, and its components can already be selected at this stage. Toward that, three pre-polymerization complexes (PPCs) consisting of CIL, FM1, or FM2, or FM3, and CLM in DCM were constructed (Section S9 in ESI†). The resulting PPC1 model containing FM1, of the highest Gibbs free energy change ΔG_C, associated with the formation of different system components ($\Delta G_C = -400.99$ kJ mol^{-1}) is shown in Fig. 1c and the less favorable models of PPC2 and PPC3 containing FM2 and FM3 (ΔG_C of -376.48 and -384.13 kJ mol^{-1}, respectively) in Fig. S1 and Scheme S1 in ESI.† All functional monomers complexed CIL quite strongly, but that formed by FM1 was the most stable. Comparing intermolecular interactions in all systems helps explain favorable complex features. Furthermore, PPC1 was selected for modeling the polymer cavity and sorption of the analytes (Fig. 1c).

3.2 Electrochemical characterizing of CIL as well as functional and cross-linking monomers

Before the electropolymerization, it is vital to determine the electro-oxidation potential of each of its components, *vis.*, the CIL template, and the functional and cross-linking monomers. This information enables choosing monomers with electro-oxidation potential lower than that of the template to avoid CIL electro-oxidation during electropolymerization. It transpired that CIL was electro-oxidized at 1.13 V *vs.* Ag quasi-reference electrode (Fig. S2a in ESI†), while the selected thiophene-appended carbazole functional and cross-linking monomers were electroactive at 0.93 and 0.92 V *vs.* Ag quasi-reference electrode, respectively (Fig. S2b and c, ESI†). These monomers have scarcely been exploited in the MIP research despite their ability of facile derivatization. Because their electro-oxidation potentials are lower than the CIL

electro-oxidation potential, they outperform pyrrole, thiophene, and phenol monomers in the electropolymerization studied.

3.3 Simultaneous depositing and characterizing MIP and NIP films

After preparing the pre-polymerization complexes in solutions, those were electropolymerized under potentiodynamic conditions to deposit MIP and NIP films on Pt electrodes (Fig. 2).

Two consecutive potential cycles were executed in the range of 0 and 1.0 V *vs.* Ag quasi-reference electrode to maintain the oxidation potential below CIL electro-oxidation potential. During the first cycle, the anodic peak was formed at 0.90 V *vs.* Ag quasi-reference electrode. In the second, one broad cathodic and one broad anodic peak emerged at potentials between 0.45 and 0.75 V and between 0.40 and 0.80 V *vs.* Ag quasi-reference electrode, respectively. The anodic peaks may arise from the formation of the cationic radicals of the deposited polymer films. Moreover, the current increase in the second cycle indicates the deposition of the increasing amounts of a conducting polymer. For NIP film deposition, the potentiodynamic behavior was similar (Fig. 2b). Notably, it was necessary to roughen the electrode surface for enhancing film adhesion. To this end, the Pt electrode was matted with 1000 grit sandpaper. Films deposited on electrodes pre-treated that way were mechanically stable.

Furthermore, successful deposition of a stable MIP film was confirmed by changes in faradaic currents using the DCM solution of the ferrocene redox probe (Fig. 2c and d). That is, CV peak-to-peak potential separation for the polymer film-coated electrode (curve 2 in Fig. 2c) was larger than that for the bare Pt electrode (curve 1 in Fig. 2c) and, consequently, the DPV peak current for the polymer film-coated electrode (curve 2′ in Fig. 2d) was significantly smaller than that for the bare Pt electrode (curve 1′ in Fig. 2d).

3.4 Characterizing deposited MIP and NIP films

Finally, the CIL template was extracted from the MIP-CIL film with 10 mM NaOH for 30 min. This extraction resulted in a significant decrease in the DPV peak current of the redox probe (Fig. 3a). The PM-IRRAS measurements were subsequently
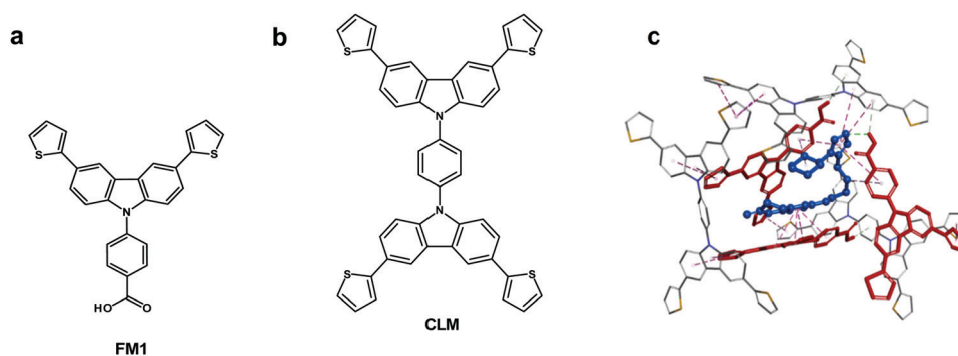

Fig. 1 The structural formula of (a) the 4-[3,6-di(thiophen-2-yl)-9*H*-carbazo-9-yl]benzoic acid functional monomer (FM1), (b) the 1,4-bis(3,6-di(thiophen-2-yl)-9*H*-carbazo-9-yl)benzene cross-linking monomer (CLM), and (c) a computer-simulated PPC1 model of the pre-polymerization complex of CIL with FM1 and CLM at the molar ratio of 1:3:3, in DCM. Important intermolecular interactions are indicated with dashed lines.
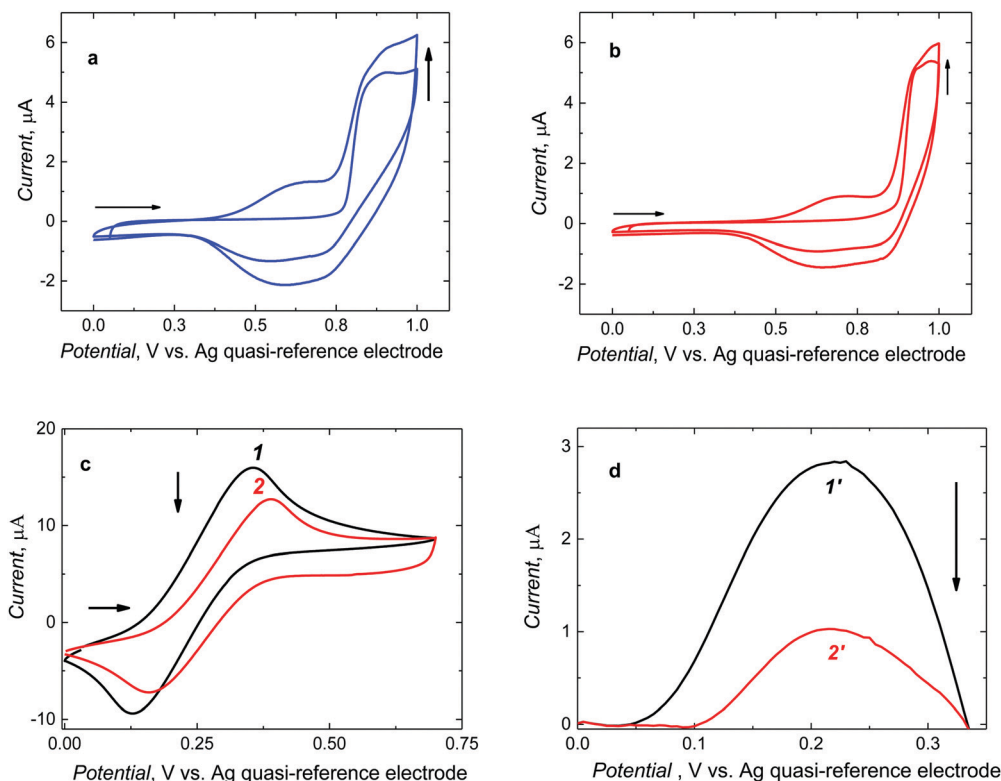
Fig. 2 Two-cycle potentiodynamic curves for deposition of (a) MIP (b) NIP films on 0.75 mm diameter Pt disk electrodes at a potential scan rate of 100 mV s^{-1}. A DCM solution of (a) 0.1 mM CIL, (a) and (b) 0.3 mM FM1, (a) and (b) 0.3 mM CLM, and 0.1 M (TBA)ClO$_4$ was used for the electropolymerization. The (c) CV and (d) background corrected DPV curves for 10 mM ferrocene and 0.1 M (TBA)ClO$_4$ in DCM on (1, 1′) the bare electrode, and (2, 2′) the MIP-CIL film-coated electrode.

performed to confirm CIL template removal from the MIP (Fig. S3 and Section S10 in ESI†). The 2-D surface topography of the films deposited on the gold film-coated glass slides was analyzed at different stages of the MIP and NIP films preparation, i.e., the electrode coated with (i) the CIL-templated MIP film, (ii) the MIP-CIL film after CIL template extraction, and (iii) the NIP film. The AFM determined MIP film thickness and roughness were 96 ($\pm$ 2) and 12.7 ($\pm$ 0.3) nm, respectively. The CIL removal from the MIP led to a further film thickness decrease to 69 ($\pm$ 5) nm while the roughness increased to 13.8 ($\pm$ 1) nm (Fig. S4, S5, and Table S1 in ESI†).

Presumably, that may indicate either removing the outermost film layer or film contracting upon CIL extraction. The as-prepared NIP film thickness and roughness were 44 ($\pm$ 6) and 9.5 ($\pm$ 0.1) nm, respectively. Moreover, after CIL extraction, the roughness of the NIP film decreased to 7.6 ($\pm$ 0.2) nm, indicating the formation of a more uniform film. Generally, both MIP and NIP films were relatively uniform, being composed of irregularly shaped grains. The average sizes of the grains were quite similar for MIP and NIP films, amounting to 87 ($\pm$ 24) and 79 ($\pm$ 20) nm, respectively. CIL template extraction affected only negligibly the grain size, equaling 86 ($\pm$ 24) and 83 ($\pm$ 22) nm for the MIP and NIP film, respectively.

Viscoelastic properties of the films were estimated based on phase angle images recorded during Tapping™ mode AFM imaging (Fig. S5 in ESI†). Notably, phase angle changes for all films were relatively uniform, thus indicating uniform film viscoelastic properties, i.e., without any significant domains of different properties. An average phase angle increase after CIL extraction indicated that the MIP film became softer. However, the NIP film was more rigid after CIL extraction, as indicated by the average phase angle decrease.

The MIP and NIP film SEM imaging results (Fig. S6 in ESI†) correlate well with AFM imaging. Moreover, these results confirmed that the films' surface was uniform.

3.5 Electrochemical CIL determining with MIP-CIL film-coated electrodes

After CIL addition to the ferrocene DCM solution, molecules of CIL interacted with complementary recognition cavities of the MIP-CIL film, thereby decreasing the DPV peak of ferrocene (Fig. 3a), as a result of the so-called "gate effect".[37,38] This current decrease was more pronounced at higher CIL concentrations (Fig. 3a, curves 1–7). However, the DPV peak current for the NIP film did not differ much after CIL addition (Fig. 3b, curves 1′-7′).

The normalized DPV peak current, $[(I_{DPV,0} - I_{DPV,s})/I_{DPV,0}$ where $I_{DPV,0}$ and $I_{DPV,s}$ stand for the initial and actual DPV peak current, respectively], was linearly dependent on the logarithm of CIL concentration within the considered concentration range. A semi-logarithmic linear regression equation of $(I_{DPV,0} - I_{DPV,s})/I_{DPV,0} = 0.32 \, (\pm 0.03) \, [1/\log \mu M] \times c_{cilostazol} \, [\log \mu M] + 0.58 \, (\pm 0.02)$

6710 | *J. Mater. Chem. B*, 2022, **10**, 6707–6715

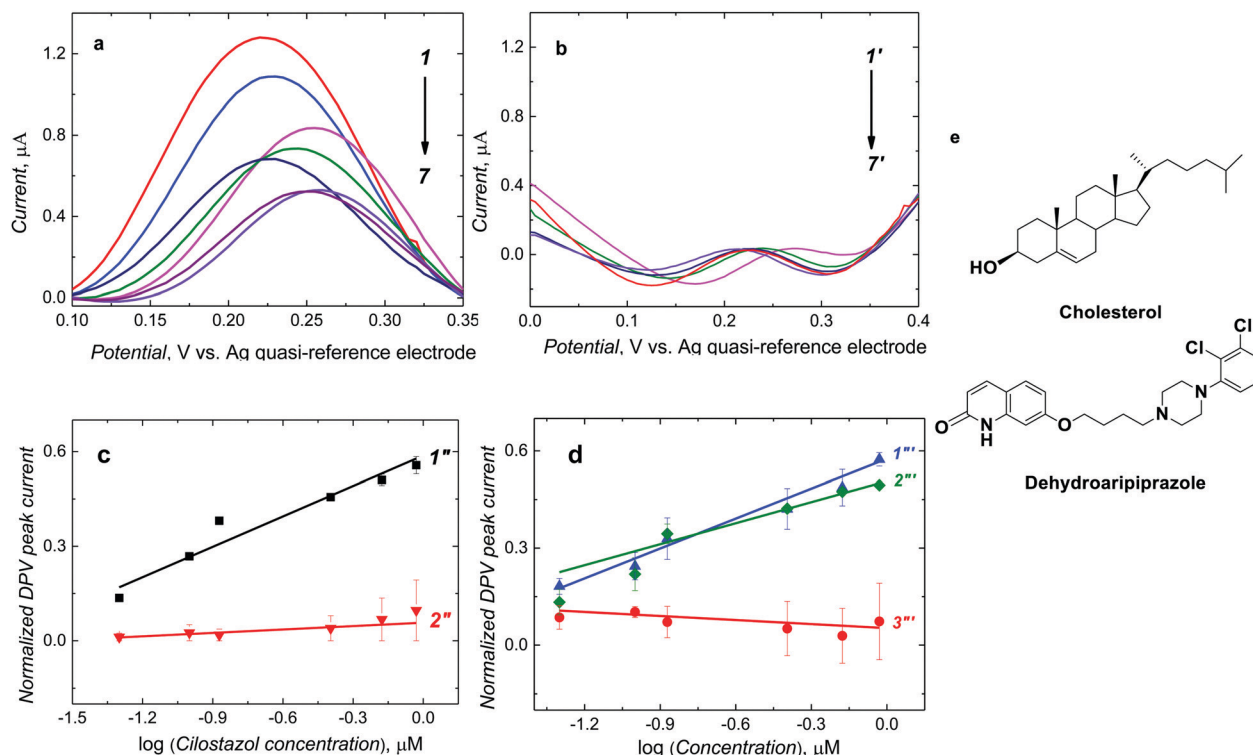This journal is © The Royal Society of Chemistry 2022

Fig. 3 Background corrected DPV curves for the (a) MIP and (b) NIP film-coated 0.75 mm diameter Pt disk electrodes (1, 1′) after CIL extraction, in (2, 2′) 50, (3, 3′) 99.8, (4, 4′) 134, (5, 5′) 402, (6, 6′) 665.9, and (7, 7′) 923.6 nM CIL in 10 mM ferrocene and 0.1 M (TBA)ClO₄ in DCM. (c) DPV calibration plots for the electrodes coated with the film of (1″) MIP-CIL and (2″) NIP. (d) DPV calibration plots for MIP-CIL film-coated electrode for (1‴) dhCIL, (2‴) cholesterol, (3‴) dehydroaripiprazole in 10 mM ferrocene and 0.1 M (TBA)ClO₄ in DCM. (e) Structural formulas of the interferences used for the selectivity tests.

describe the calibration plot (Fig. 3c, curve 1″). The correlation coefficient and sensitivity were R^2 = 0.927 and 0.32 (± 0.03) [1/log μM], respectively. A linear dynamic concentration range extended from 50 to 923.6 nM CIL with the LOD of 15 nM.

In the case of the NIP film-coated electrode, the normalized DPV peak currents for CIL at similar concentrations were smaller (Fig. 3c, curve 2″). The sensitivity was 0.03 (± 0.01) [1/log μM]. This result indirectly confirms the successful imprinting of molecular cavities in the MIP. Accordingly, the apparent imprinting factor was relatively high, IF = 10.6. It was calculated as the ratio of slopes of calibration plots for the MIP and NIP film-coated electrodes. Common interferences encountered in body fluids (Fig. 3e) were used to perform the cross-reactivity studies for estimating the molecular recognition's selectivity of the MIPs. Experimental selectivity was determined as the ratio of the slope of the calibration plot of the MIP film chemosensor for CIL to that of dhCIL or that of any interference. Advantageously, the selectivity for the dhCIL was very low, vis., ∼1.06 (Fig. 3d, curve 1‴) indicating that the chemosensor is not selective to dhCIL and this metabolite is likely to be determined together with CIL. That is understandable because of the only minor difference in the CIL and dhCIL structures (Scheme 1). Interestingly, the selectivity for structurally similar dehydroaripiprazole analog (Fig. 3d, curve 3‴) was also high, equaling 8.00. However, a low selectivity of 1.52 determined for cholesterol (Fig. 3d, curve 2‴) indicates

that the chemosensor is weakly selective to this interference, presumably, because its molecule is smaller than the CIL molecule and, therefore, can easily penetrate the cavity.

For repeatability study, CIL was determined in 50 nM CIL using five different MIP chemosensors. The DPV peak response was 1.00 (± 0.10) μA demonstrating relatively high chemosensor repeatability.

3.6 Chemosensor analytical performance in CIL or dhCIL spiked human plasma samples

Estimating the matrix effect on the chemosensor's performance is crucial for analyte determination in real samples. With that respect, an MIP film-coated electrode was applied for CIL determination in human plasma. The plasma samples spiked with CIL of known concentration, determined with LC-MS, were thawed in air and then diluted with DCM.

Remarkably, the chemosensor determined CIL and dhCIL successfully in spiked human plasma, with high recovery (Table 2). Notably, the devised chemosensor analytical parameters favorably compare with those of already known chemosensors (Table S4 in ESI†). The LOD is lower, but the linear dynamic concentration range is broader only for the luminescence-based sensor. However, this sensor was devised for CIL determination in pharmaceutical formulations and was not tested for real plasma samples. Therefore, no biological matrix effect was studied. Moreover, the determination procedure described herein is less

This journal is © The Royal Society of Chemistry 2022

J. Mater. Chem. B, 2022, 10, 6707–6715 | 6711

Table 1 The determined MIP-CIL cavity selectivity to the CIL metabolite, dhCIL, and interferences, and calculated changes of the Gibbs free energy (ΔG_{bind}) accompanying the MIP-CIL model cavity complexation of dhCIL and the interferences

Guest compound	Experimental selectivity, DPV	Calculated ΔG_{bind}, kJ mol^{-1}
Cilostazol (CIL)	—	−159.29
3,4-Dehydrocilostazol (dhCIL)	∼1.06	−153.77
Cholesterol	1.52	−140.75
Dehydroaripiprazole	8.00	−90.74

demanding than that needed for luminescence-based chemosensing. Furthermore, the efforts were extended here to determine the parameters of CIL binding by the MIP-CIL film. Typically, Langmuir (L), Freundlich (F), and Langmuir–Freundlich (LF) isotherms most accurately describe this binding.[39] Therefore, these three isotherms were tested herein to describe the normalized ferrocene DPV peak current dependence on the CIL concentration in the ferrocene DCM solution (Fig. S7 and Table S2a and b in ESI†). The LF isotherm fit to the data acquired was the best, meaning that CIL molecules predominantly interact with the imprinted cavities and not mutually with themselves and that cavity distribution is to some extent heterogenic. The homogeneity factor (n) exceeding 1, determined, indicates that the sorption is favorable (Table S3 in ESI†). Moreover, the binding constant (K_{LF}) calculated is reasonably high.

3.7 Chemosensor selectivity

The chemosensor application for analyte determination in real samples should be selective to interferences. This issue can be modeled by simulating the analyte and interferences binding by the MIP. To this end, the cavity in the MIP-CIL model was simulated based on the PPC1 complex structure (Section S8 in ESI†). In this model, the cavity is treated as the host for binding, separately, molecules of all guest compounds tested. Fig. 4a and b present molecular structures of the cavity and the distribution of the molecular electrostatic potential (MEP) on its surface generated by the FM1 and CLM molecules. The neutral potential is located deep inside the cavity, while the regions with the negative (red) to positive (blue) potentials are close to the cavity edge, in heteroatoms proximity. The binding was simulated for CIL and dhCIL analytes as well as cholesterol and dehydroaripiprazole interferences (Section S8 in ESI†) to assess the chemosensor selectivity. The optimized structures of the cavity interacting with the above guest molecules are presented in Fig. 4c, d, and Fig. S8 in ESI.† The calculated Gibbs free energy change (ΔG_{bind}) and the experimental selectivity of the MIP-CIL to each guest compound studied are compared in Table 1. Apparently, the predicted MIP cavities' affinities to CIL and dhCIL are high and similar, whereas affinities to dehydroaripiprazole and cholesterol are much lower.

The interactions within the cavity and localization of guest molecules can explain the differences in the affinities. CIL and dhCIL molecules are located in similar cavity regions, and their conformations are almost identical. Hence, the intermolecular interactions are similar (Fig. S8d in ESI†). To summarize, the MIP-CIL can be proposed as the recognition unit of a chemosensor for selective CIL and dhCIL determination in the presence of the cholesterol and dehydroaripiprazole interferences.

Table 2 Comparison of CIL and dhCIL methods of determination in CIL spiked human plasma and a test solution using LC-MS and the MIP-CIL chemosensor

| Sample no.	LC-MS determined CIL in the test solution, nM	LC-MS determined CIL in human plasma, nM[a]	Recovery, %	CIL concentration in the test solution, nM	MIP chemosensor determined CIL in the test solution, nM	Recovery, %
1	27.1	28.6	105.5	27.1	27.2 (± 4.5)	100.3 (± 16.6)
2	81.2	88.2	108.6	81.2	80.7 (± 3.9)	99.3 (± 4.8)
3	676.7	717.4	106.0	676.7	734.0 (± 3.1)	108.4 (± 0.4)
4	3518.6	3500	99.4	351.8	354.0 (± 4.5)	100.6 (± 1.3)
5	8120.0	7626.5	93.9	812.0	1088.9 (± 13.4)	134.1 (± 1.6)
3,4-Dehydrocilostazol	81.6	89.8	110.0	81.6	89.5 (± 1.4)	109.6 (± 1.7)

[a] Arithmetic average (n = 6).
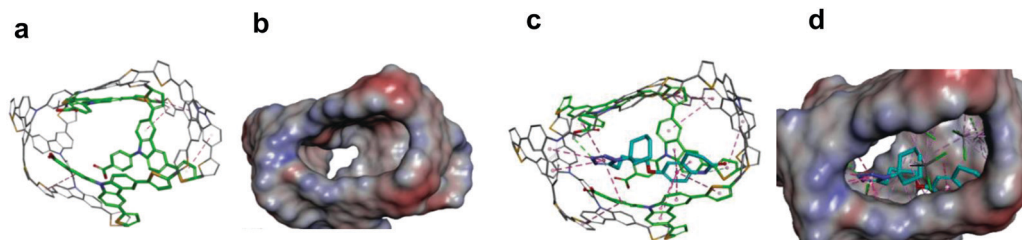
Fig. 4 Computer simulated structures of the molecular cavity in MIP-CIL (a) The skeleton model, (b) surface distribution of molecular electrostatic potential (MEP) colored according to the interpolated (blue) positive and (red) negative charge, (c) the skeleton model of the cavity with CIL molecule entrapped showing intermolecular interactions, and (d) the cavity with CIL molecule entrapped showing interactions with dichloromethane.

6712 | *J. Mater. Chem. B*, 2022, **10**, 6707–6715

This journal is © The Royal Society of Chemistry 2022

3.8 Solvent impact on intermolecular interactions

For a non-covalently imprinted polymer synthesizing, a porogen solvent is an essential factor affecting the pre-polymerization complex formation and then sorption of the analyte or interferences in the resulting MIP molecular cavities.[40] The herein adopted simulation strategy considering the solvent in imprinting revealed the DCM molecules' participation in intermolecular interactions with molecules of the CIL template, the FM1, and CLM monomers, and interferences (Section S11 in ESI†). These interactions are illustrated with the sorption models (Fig. 4 and Figure S9 of ESI†).

4. Conclusions

The chosen electroactive thiophene-appended carbazole functional and cross-linking monomers appeared effective in CIL molecular imprinting in a polymer. The MIP thin film prepared checked itself as the recognition unit of an electrochemical chemosensor for selective CIL determination in human plasma. Its apparent imprinting factor was as high as IF = 10.6, indicating efficient imprinting. The DPV normalized peak current for the ferrocene redox probe dependence on the logarithm of cilostazol concentration was linear between 50 and 924 nM CIL. The attained limit of detection of 15 nM CIL is well below the cut-off 135 nM CIL adopted in clinical practice (Table S4 in ESI†). Therefore, the chemosensor seems promising for use in clinical analysis.

Moreover, it is an excellent candidate for point-of-care (PoC) applications because of the short ($<$5 min) time of CIL determination, disposability, operation simplicity, repeatability, and low cost, all essential in monitoring the patient's response to treatment at home. Furthermore, the chemosensor response to the dhCIL active primary metabolite of CIL is nearly identical to that of the CIL analyte. Therefore, beneficially, they can be determined together. Advantageously, the chemosensor is highly selective to dehydroaripiprazole interference. However, it is not selective to cholesterol, presumably because its molecular size is smaller than that of the CIL molecule. Hence, molecules of cholesterol can readily enter to become entrapped in the CIL-imprinted cavities. Therefore, cholesterol should be pre-removed from clinical samples. As a very lipophilic substance, it can readily be extracted with highly non-polar solvents, *e.g.*, aliphatic hydrocarbons that do not dissolve polar CIL and dhCIL. Fitting the selected isotherms to the sorption data indicated the formation of molecular cavities imprinted in the MIP and these cavities' strong CIL binding. Binding sites distribution in the MIP is somewhat non-homogeneous. Notably, fitting the isotherms for the NIP revealed significantly weaker and relatively homogeneous binding of non-interacting molecules. Computational simulations allowed selecting the most appropriate monomers for the MIP synthesis. The theoretical binding model explained the differences in chemosensor selectivity and emphasized the DCM solvent role in the intermolecular interaction.

Author contributions

Conflicts of interest

There are no conflicts to declare.

Acknowledgements

References

1 T. Mueller, F. Hinterreiter, C. Luft, W. Poelz, M. Haltmayer and B. Dieplinger, Mortality Rates and Mortality Predictors in Patients with Symptomatic Peripheral Artery Disease Stratified According to Age and Diabetes, *J. Vasc. Surg.*, 2014, **59**(5), 1291–1299.

2 J. Shu and G. Santulli, Update on Peripheral Artery Disease: Epidemiology and Evidence-Based Facts, *Atherosclerosis*, 2018, **275**, 379–381.

3 J.-R. Kim, J. A. Jung, S. Kim, W. Huh, J.-L. Ghim, J.-G. Shin and J.-W. Ko, Effect of Cilostazol on the Pharmacokinetics of Simvastatin in Healthy Subjects, *BioMed Res. Int.*, 2019, 1–6.

4 S. Take, M. Matsutani, H. Ueda, H. Hamaguchi, H. Konishi, Y. Baba, H. Kawaratani, T. Sugiura, T. Iwasaka and M. Inada, Effect of Cilostazol in Preventing Restenosis After Percutaneous Transluminal Coronary Angioplasty, *Am. J. Cardiol.*, 1997, **79**(8), 1097–1099.

5 S. L. Bramer, P. N. V. Tata and S. Mallikaarjun, Disposition of 14 C-Cilostazol after Single Dose Administration to Healthy Human Subjects, *Pharm. Res.*, 1997, **14**, S612.

6 H. Sakurai, H. Hanyu, T. Sato, K. Kume, K. Hirao, H. Kanetaka, T. Iwamoto, K. Ono, M. Tsuji, N. Hishikawa, Y. Fukui, K. Sato, Y. Ohta, T. Yamashita, K. Abe, S. Saito and M. Ihara, Effects of Cilostazol on Cognition and Regional Cerebral Blood Flow in Patients with Alzheimer's Disease and Cerebrovascular Disease: A Pilot Study, *Geriatr. Gerontol. Int.*, 2017, **6**(1), 1384–1391.

7 W. S. Weintraub, The Vascular Effects of Cilostazol, *Can. J. Cardiol.*, 2006, **22**(suppl. B), 56B–60B.

8 M. Di Napoli, P. Singh, S. Lattanzi and A. A. Divani, The Use of Cilostazol for Secondary Stroke Prevention: Isn't Time to Be Evaluated in Western Countries?, *Expert Opin. Pharmacother.*, 2020, **21**(4), 381–387.

9 M. Sahin, E. Alizade, S. Pala, G. Alici, B. Ozkan, T. Akgun, Y. Emiroglu, S. Demir, M. V. Yazicioglu and M. M. Turkmen, The Effect of Cilostazol on Right Heart Function and Pulmonary Pressure, *Cardiovasc. Ther.*, 2013, **31**(6), e88–e93.

10 D. L. Dawson, B. S. Cutler, W. R. Hiatt, R. W. Hobson, J. D. Martin, E. B. Bortey, W. P. Forbes and D. E. Strandness, A Comparison of Cilostazol and Pentoxifylline for Treating Intermittent Claudication, *Am. J. Med.*, 2000, **109**(7), 523–530.

11 M. E. O'Donnell, S. A. Badger, M. A. Sharif, I. S. Young, B. Lee and C. V. Soong, The Vascular and Biochemical Effects of Cilostazol in Patients with Peripheral Arterial Disease, *J. Vasc. Surg.*, 2009, **49**(5), 1226–1234.

12 S. L. Bramer, W. P. Forbes and S. Mallikaarjun, Cilostazol Pharmacokinetics after Single and Multiple Oral Doses in Healthy Males and Patients with Intermittent Claudication Resulting from Peripheral Arterial Disease, *Clin. Pharmacokinet.*, 1999, **37**(SUPPL. 2), 1–11.

13 H. Akiyama, S. Kudo and T. Shimizu, The Absorption, Distribution and Excretion of a New Antithrombotic and Vasodilating Agent, Cilostazol, in Rat, Rabbit, Dog and Man, *Arzneimittelforschung*, 1985, **35**(7A), 1124–1132.

14 Z. S. Ballard, H. A. Joung, A. Goncharov, J. Liang, K. Nugroho, D. Di Carlo, O. B. Garner and A. Ozcan, Deep Learning-Enabled Point-of-Care Sensing Using Multiplexed Paper-Based Sensors, *npj Digit. Med.*, 2020, **3**(66), 1–8.

15 Y. Manmana, T. Kubo and K. Otsuka, Recent Developments of Point-of-Care (POC) Testing Platform for Biomolecules, *TrAC, Trends Anal. Chem.*, 2021, **135**, 116160.

16 J. Canals, N. Franch, O. Alonso, A. Vilà and A. Diéguez, A Point-of-Care Device for Molecular Diagnosis Based on CMOS SPAD Detectors with Integrated Microfluidics, *Sensors*, 2019, **19**(3), 445.

17 C. S. Kosack, A. L. Page and P. R. Klatser, A Guide to Aid the Selection of Diagnostic Tests, *Bull. W. H. O.*, 2017, **95**(9), 639–645.

18 E. Amalfitano, M. Karlikow, M. Norouzi, K. Jaenes, S. Cicek, F. Masum, P. Sadat Mousavi, Y. Guo, L. Tang, A. Sydor, D. Ma, J. D. Pearson, D. Trcka, M. Pinette, A. Ambagala, S. Babiuk, B. Pickering, J. Wrana, R. Bremner, T. Mazzulli, D. Sinton, J. H. Brumell, A. A. Green and K. Pardee, A Glucose Meter Interface for Point-of-Care Gene Circuit-Based Diagnostics, *Nat. Commun.*, 2021, **12**(1), 1–10.

19 P. B. Luppa, Point-of-Care Testing at the Interface of Emerging Technologies and New Clinical Applications, *J. Lab. Med.*, 2020, **44**(2), 59–61.

20 D. J. Denmark, S. Mohapatra and S. S. Mohapatra, Point-of-Care Diagnostics: Molecularly Imprinted Polymers and Nanomaterials for Enhanced Biosensor Selectivity and Transduction, *EuroBiotech J.*, 2020, **4**(4), 184–206.

21 F. Cui, Z. Zhou and H. S. Zhou, Molecularly Imprinted Polymers and Surface Imprinted Polymers Based Electrochemical Biosensor for Infectious Diseases, *Sensors*, 2020, **20**(4), 996.

22 R. Xing, S. Wang, Z. Bie, H. He and Z. Liu, Preparation of Molecularly Imprinted Polymers Specific to Glycoproteins, Glycans and Monosaccharides via Boronate Affinity Controllable-Oriented Surface Imprinting, *Nat. Protoc.*, 2017, **12**(5), 964–987.

23 H. Dai, D. Xiao, H. He, H. Li, D. Yuan and C. Zhang, Synthesis and Analytical Applications of Molecularly Imprinted Polymers on the Surface of Carbon Nanotubes: A Review, *Microchim. Acta*, 2015, **182**(5), 893–908.

24 O. S. Ahmad, T. S. Bedwell, C. Esen, A. Garcia-Cruz and S. A. Piletsky, Molecularly Imprinted Polymers in Electrochemical and Optical Sensors, *Trends Biotechnol.*, 2019, **37**(3), 294–309.

25 S. A. Zaidi, Molecular Imprinted Polymers as Drug Delivery Vehicles, *Drug Delivery*, 2016, **23**(7), 2262–2271.

26 M. Peeters; K. Eersels; T. Junkers and P. Wagner, Molecularly Imprinted Polymers: Synthetic Receptors for Diagnostic Medical Devices, in *Molecularly Imprinted Catalysts – Principles, Syntheses, and Applications*, ed. S. Li, S. Cao, S. A. Piletsky and A. P. F. Turner, Elsevier, Amsterdam, 2016, pp. 253–271.

27 X. Liu, X. Wang, F. Tan, H. Zhao, X. Quan, J. Chen and L. Li, An Electrochemically Enhanced Solid-Phase Microextraction Approach Based on Molecularly Imprinted Polypyrrole/Multi-Walled Carbon Nanotubes Composite Coating for Selective Extraction of Fluoroquinolones in Aqueous Samples, *Anal. Chim. Acta*, 2012, **727**, 26–33.

28 R. Gao, X. Su, X. He, L. Chen and Y. Zhang, Preparation and Characterisation of Core–Shell CNTs@MIPs Nanocomposites and Selective Removal of Estrone from Water Samples, *Talanta*, 2011, **83**(3), 757–764.

29 N. M. Bhatt, V. D. Chavada, D. P. Patel, P. Sharma, M. Sanyal and P. S. Shrivastav, Determination of Cilostazol and Its Active Metabolite 3,4-Dehydro Cilostazol from Small Plasma Volume by UPLC-MS/MS, *J. Pharm. Anal.*, 2015, **5**(1), 1–11.

30 S. L. Bramer, P. N. V. Tata, S. S. Vengurlekar and J. H. Brisson, Method for the Quantitative Analysis of Cilostazol and Its Metabolites in Human Plasma Using LC/MS/MS, *J. Pharm. Biomed. Anal.*, 2001, **26**, 637–650.

31 M. L. S. Gomes, T. Klein, M. Simionatto, J. M. Nadal, S. M. W. Zanin, D. M. Borsato and P. V. Farago, A Simple RP-HPLC/UV Method for Determination of Cilostazol in Polymeric Nanoparticles Suspensions: Development and Validation, *Lat. Am. J. Pharm.*, 2015, **34**(4), 803–809.

32 F. Ibrahim, M. S. El-din and H. A. El-Aziz, New Validated Fluorescence Quenching Based Procedure for the Determination of Cilostazol and Clopidogrel in Bulk, Tablets and Biological Fluids, With Application of Stern–Volmer Equation, *Br. J. Pharm. Res.*, 2016, **12**(6), 1–15.

33 M. S. Attia, W. H. Mahmoud, A. O. Youssef and M. S. Mostafa, Cilostazol Determination by the Enhancement of

6714 | *J. Mater. Chem. B*, 2022, **10**, 6707–6715

This journal is © The Royal Society of Chemistry 2022

the Green Emission of Tb[3+] Optical Sensor, *J. Fluoresc.*, 2011, **21**(6), 2229–2235.

34 A. Kidakova, J. Reut, R. Boroznjak, A. Öpik and V. Syritski, Advanced Sensing Materials Based on Molecularly Imprinted Polymers towards Developing Point-of-Care Diagnostics Devices, *Proc. Est. Acad. Sci.*, 2019, **68**(2), 158–167.

35 N. Afsarimanesh, S. C. Mukhopadhyay and M. Kruger, *Electrochemical Biosensor: Point-of-Care for Early Detection of Bone Loss*, ed. S. C. Mukhopadhyay, Springer Nature, Switzerland, 1st edn, 2019, vol. 30.

36 Jyoti, C. Gonzato, T. Żołek, D. Maciejewska, A. Kutner, F. Merlier, K. Haupt, P. S. Sharma, K. R. Noworyta and W. Kutner, Molecularly Imprinted Polymer Nanoparticles-Based Electrochemical Chemosensors for Selective Determination of Cilostazol and Its Pharmacologically Active Primary Metabolite in Human Plasma, *Biosens. Bioelectron.*, 2021, **193**, 113542.

37 P. S. Sharma, A. Garcia-Cruz, M. Cieplak, K. R. Noworyta and W. Kutner, 'Gate Effect' in Molecularly Imprinted Polymers: The Current State of Understanding, *Curr. Opin. Electrochem.*, 2019, **16**, 50–56.

38 Y. Yoshimi, R. Ohdaira, C. Iiyama and K. Sakai, 'Gate Effect' of Thin Layer of Molecularly-Imprinted Poly(Methacrylic Acid-Co-Ethyleneglycol Dimethacrylate), *Sens. Actuators, B*, 2001, **73**(1), 49–53.

39 R. J. Umpleby, S. C. Baxter, A. M. Rampey, G. T. Rushton, Y. Chen and K. D. Shimizu, Characterization of the Heterogeneous Binding Site Affinity Distributions in Molecularly Imprinted Polymers, *J. Chromatogr. B: Anal. Technol. Biomed. Life Sci.*, 2004, **804**(1), 141–149.

40 B. Zhang, X. Fan and D. Zhao, Computer-Aided Design of Molecularly Imprinted Polymers for Simultaneous Detection of Clenbuterol and Its Metabolites, *Polymers*, 2019, **11**(1), 17.